Biosensors and Bioelectronics 66 (2015) 198–207

Contents lists available at ScienceDirect

Biosensors and Bioelectronics

journal homepage: www.elsevier.com/locate/bios

A sensitive and selective magnetic graphene composite-modified polycrystalline-silicon nanowire field-effect transistor for bladder cancer diagnosis

Hsiao-Chien Chen [a,b,c,1], Yi-Ting Chen [d,1], Rung-Ywan Tsai [e], Min-Cheng Chen [f], Shi-Liang Chen [a,b,g], Min-Cong Xiao [a,b,g], Chien-Lun Chen [h], Mu-Yi Hua [a,b,g,*]

[a] Department of Chemical and Materials Engineering, Chang Gung University, Taoyuan 33302, Taiwan, ROC
[b] Biosensor Group, Biomedical Engineering Research Center, Chang Gung University, Taoyuan 33302, Taiwan, ROC
[c] Department of Biochemistry and Molecular Cell Biology, School of Medicine, College of Medicine, Taipei Medical University, Taipei 11031, Taiwan, ROC
[d] Department of Biomedical Sciences, College of Medicine, Chang Gung University, Taoyuan 33302, Taiwan, ROC
[e] Electronics and Optoelectronics Research Laboratories, Industrial Technology Research Institute, Hsinchu 310, Taiwan, ROC
[f] National Nano Device Laboratories, Hsinchu Science Park, Hsinchu 31040, Taiwan, ROC
[g] Green Technology Research Center, Chang Gung University, Taoyuan 33302, Taiwan, ROC
[h] Department of Urology, Chang Gung University College of Medicine and Memorial Hospital, Taoyuan 33305, Taiwan, ROC

ARTICLE INFO

Article history:
Received 14 September 2014
Received in revised form
12 November 2014
Accepted 16 November 2014
Available online 18 November 2014

Keywords:
Graphene
FET
Bladder cancer
Biosensor
Apolipoprotein A II protein

ABSTRACT

In this study, we describe the urinary quantification of apolipoprotein A II protein (APOA2 protein), a biomarker for the diagnosis of bladder cancer, using an n-type polycrystalline silicon nanowire field-effect transistor (poly-SiNW-FET). The modification of poly-SiNW-FET by magnetic graphene with long-chain acid groups (MGLA) synthesized *via* Friedel–Crafts acylation was compared with that obtained using short-chain acid groups (MGSA). Compared with MGSA, the MGLA showed a higher immobilization degree and bioactivity to the anti-APOA2 antibody (Ab) due to its lower steric hindrance. In addition, the magnetic properties enabled rapid separation and purification during Ab immobilization, ultimately preserving its bioactivity. The Ab-MGLA/poly-SiNW-FET exhibited a linear dependence of relative response to the logarithmical concentration in a range between 19.5 pg mL^{-1} and 1.95 μg mL^{-1}, with a limit of detection (LOD) of 6.7 pg mL^{-1}. An additional washing step before measurement aimed at excluding the interfering biocomponents ensured the reliability of the assay. We conclude that our biosensor efficiently distinguishes mean values of urinary APOA2 protein concentrations between patients with bladder cancer (29–344 ng mL^{-1}) and those with hernia (0.425–9.47 ng mL^{-1}).

1. Introduction

Among men and women in the Western world, bladder cancer is the fourth and eighth most common malignancy, respectively. Bladder cancer occurs in the epithelial lining of the bladder (Kirkali et al., 2005). Non-muscle-invasive bladder cancer occurs in approximately 70% of bladder cancer incidents. High-grade stages of muscle-invasive bladder cancer are associated with significant tumor progression and, consequently, increased mortality. Therefore, to determine the optimal treatment, it is critical to accurately detect bladder cancer at an early stage. Traditionally, diagnosis is a complex process based on the experience of a urologist, radiologist or cytopathologist. Diagnostic approaches include cystoscopy, which is invasive and therefore painful, and urine cytology, which is not sufficiently sensitive for the detection of low-grade stages (Araki et al., 2007).

A good biomarker reflects various conditions of a biological system and enables better disease diagnosis and/or treatment outcomes. The biomedical field is highly interested in the development of disease biomarkers, where the biomarker development pipeline generally comprises three stages, which include biomarker discovery, verification, and clinical validation (Surinova et al., 2011). The process usually begins with biomarker discovery based on a limited number of cases and uses deep profiling, which can achieve the identification of thousands of proteins in a biological sample. Prior to the application of potential biomarker candidates in translational medicine, the candidates must be evaluated in 100–1000 samples in the verification and validation phases using high-throughput, sensitive assays. A variety of

* Corresponding author at: Department of Chemical and Materials Engineering, Chang Gung University, Taoyuan 33302, Taiwan, ROC. Fax: +886 3 2118668.
E-mail address: huamy@mail.cgu.edu.tw (M.-Y. Hua).
[1] H.-C. Chen and Y.-T. Chen contributed equally to this work.

http://dx.doi.org/10.1016/j.bios.2014.11.019
0956-5663/

diagnostic tests have been investigated for the detection of bladder cancer. Valid, reliable and inexpensive tests that can be easily and rapidly performed include Raman spectroscopy for diagnosing urothelial carcinoma cell (Shapiro et al., 2011), elastic light scattering for detecting papillary transitional cell carcinoma (Mourant et al., 1995), polymerase chain reaction for telomerase detection (Kim et al., 2013), enzyme-linked immunosorbent assay (ELISA) for MUC1 detection (Ferreira et al., 2008), silicon microring resonators for monitoring fibroblast growth factor receptor 3 and Harvey RAS, nuclear magnetic resonance for measurements of leucine, tyrosine, lactate, glycine and citrate (Cao et al., 2012), electrochemistry for H_2O_2 detection (Hua et al., 2011a; Roberts et al., 2013), chromatography for detecting carnitine C9:1 (Kałuzna-Czaplinska and Jóźwik, 2014), and surface plasmon resonance for Her-2 determination (Tai et al., 2007). Additionally, a variety of candidate bladder cancer biomarkers such as RT112 cell CDH1, FHIT, LAMC2, RASSF1A, TIMP3, SFRP1, SOX9, PMF1 and RUNX3 have been identified but require further validation (Roberts et al., 2013; Shin et al., 2013; Kandimalla et al., 2013). Apolipoprotein A-IIprotein (APOA2) was recently identified as a new biomarker that occurs a highly elevated rates in pooled bladder cancer. The relative difference in the level of APOA2 protein in urine is a highly significant factor (Chen et al., 2010, 2012).

The use of field-effect transistors (FETs) to diagnose bladder cancer from urine specimens has not been reported. Due to the associated advantages of miniaturization and superior sensitivity, significant effort has been expended toward the development of FET biosensors in recent years (Kwon et al., 2012; Lee et al., 2009). High selectivity is achieved by immobilizing antibodies, peptides, and oligonucleotide-based aptamers to bind specific molecules. In this configuration, the binding analyte affects the channel conductivity in a manner that is similar to the effect of voltage application to a metallic gate electrode. However, earlier FETs with planar or two-dimensional surfaces exhibited low sensitivity, limiting their application, particularly for trace analytes. One-dimensional FET channels with nanostructures of nanowires (Li et al., 2013; Chen et al., 2011), graphene (Trung et al., 2014), nanobelts (Oh et al., 2013) or nanotubes (Chen et al., 2014) are extremely attractive due to the depletion or accumulation of carriers in the bulk of the nanoscale structures.

Magnetic and gold nanoparticles are loaded in the channels to increase the surface area, thereby increasing the quantity of immobilized biomolecules (Chen et al., 2014; Allen et al., 2007). Graphene sheets (Gs) are a potential candidate for the modification of SiNW-FETs due to the inherently high surface area and superior conductivity (Sykes and Charles, 2009). However, Gs lack functional groups for the immobilization of biomolecules, thus it is necessary to chemically modify Gs. The best-known functionalization of Gs is Hummers' chemical modification, in which treatment with a strong acid and an oxidant is used to produce various oxygen-containing groups, including short-chain carboxylic acids (Liu et al., 2008). The carboxylic acid group can subsequently form covalent bonds with amine-containing biomolecules *via* the EDC/sulfo-NHS reaction. However, fewer investigations have focused on the effects of chain length on the degree of biomolecule loading and the associated role of steric hindrance. To clarify the effect of the carboxylic acid chain length, Gs with a four-carbon-chain carboxylic acid group were synthesized *via* Friedel–Crafts acylation and compared with the product of Hummers' chemical modification in this study. Additionally, magnetic nanoparticles of Fe_3O_4 were synthesized *in situ* on the carboxylated Gs to enable rapid purification. After immobilizing anti-APOA2 on the magnetic carboxylated Gs and loading on the poly-SiNW-FET channel, a novel bladder cancer biosensor was developed based on a poly-SiNW-FET device. Performing an additional washing process ensured the accuracy of the biosensor measurement by eliminating other charged species. Finally, individual urine samples from age-matched hernia patients and bladder cancer patients were analyzed using the proposed biosensor; the results clearly indicated that the biosensor can distinguish among these two sample types. These results demonstrate that bladder cancer diagnosis is feasible using a modified poly-SiNW-FET device.

2. Experiments

2.1. Patients and materials

Clinical specimens were collected using a previously described protocol (Chen et al., 2010, 2012). Briefly, first-morning urine samples were collected from hernia patient controls and bladder cancer patients into containers that contained a protease inhibitor cocktail tablet (one tablet per 50 mL of urine; Roche, Mannheim, Germany) and sodium azide (1 mM). As controls, first-morning urine samples were collected from hernia patients of comparable age using an identical procedure after admission and before surgical intervention. The collected urine samples were centrifuged at $5000 \times g$ for 30 min at 4 °C within 5 h of collection to remove cells and debris, and the clarified supernatants were stored at −80 °C until further processing. All clinical samples were collected from the Department of Urology, Chang Gung Memorial Hospital, Taoyuan, Taiwan. This study was approved by the Ethics Committee of Chang Gung Memorial Hospital (IRB nos. 102-3232A3 and 99-2188B). All subjects received a description of the study and provided written informed consent. APOA2 and anti-APOA2 were obtained from Abcam, CB, UK. Maleic anhydride (MA) was purchased from TCI. *N*-hydroxysulfo-succinimide sodium salt (sulfo-NHS) was purchased from Fluka. PBS, EDC, goat anti-human IgG (Fc specific)-peroxidase antibody, BSA and MES buffer (pH 6.3) were purchased from Sigma. Acetone, methanol, and 1-methyl-2-pyrrolidone (NMP) were purchased from Tedia. Aluminum chloride and TBO were purchased from Acros, and graphite was purchased from Alfa Aesar. NaOH, $FeCl_2$ and $FeCl_3$ were purchased from Merck.

2.2. Syntheses of GLA and GSA

A 50 mg quantity of graphite as temporarily dispersed in 10 mL of anhydrous NMP with sonication. One gram of MA was dissolved in 40 mL of anhydrous NMP solution under nitrogen, and $AlCl_3$ was then added at a molar ratio of 1:1, 1:3, or 1:6 at 90 °C. After stirring for 3 h, the graphite solution was added to the three MA–$AlCl_3$ solutions and reacted at 160 °C for 48 h. The samples were filtered through 0.1-μm PVDF membranes and washed with methanol and DI water 3 times. The yellow solutions were collected after centrifugation at 3000 rpm. Finally, the products were obtained from the filter cake by filtration through a 0.1-μm PVDF membrane, and the products were labeled GLA11, GLA13, and GLA16. GSA was synthesized from expandable graphite flake using a method modified from Hummer (Liu et al., 2008).

2.3. Syntheses of MGLA and MGSA

A 200-mg quantity of GLA was dispersed in 20 mL of DI water. $FeCl_3$ (4.32 mmol) and $FeCl_2 \cdot 4H_2O$ (6.48 mmol) were dissolved in 380 mL of DI water at room temperature and mixed with the GLA solution under N_2 gas. After heating this solution slowly to 50 °C, and 30 mL of NaOH (0.576 N) was slowly added over 20 min, resulting in a final temperature of 80 °C. The reaction was then rapidly quenched on ice, and 0.1 N HCl was slowly added until a neutral pH was obtained. MGLA was separated from the solution *via* the application of a magnetic field and then was washed with

DI water several times. MGSA was prepared according to the method described above.

2.4. Preparation of Ab-MGLA and Ab-MGSA

EDC (50 mg) and sulfo-NHS (60 mg) were dissolved in 5 mL of MES in the dark. A 0.2-mL aliquot of this solution was mixed with 0.1 mL of MGLA (10 μg mL^{-1}) at 25 °C with shaking for 30 min in the dark. After separation by the application of a magnetic field, the MGLA was washed with 0.8 mL of MES, re-suspended in 0.2 mL of MES, and mixed with 10, 25, 50, 100, 150 or 200 ng of anti-APOA2 at 25 °C for 3 h. Ab-MGLA was separated from the solution and washed with PBS to remove free anti-APOA2. Ab-MGSA was prepared as described above, except that 0.1 mL of MGSA (21.3 μg mL^{-1}) was used.

2.5. ELISA assay for anti-APOA2 quantification

300, 150, 75, 37.5, 18.8, 9.4, 4.7 and 2.3 ng mL^{-1} of anti-APOA2 (150 μL) were coated on Microlite 2 multiwell plates (Thermo Labsystems, Franklin, MA) for 1.5 h. After washing with PBS, 150 μL of BSA (5 mg mL^{-1}) were used as block for 1.5 h before hybridization with 1.95 μg mL^{-1} of APOA2 protein (150 μL) for 1.5 h. A total of 150 μL of BSA (5 mg mL^{-1}) were utilized for further blocking. 100 μL of biotin-antibody was added to each well and incubated for 1 h at 37 °C. After removing the solution, 90 μL of TMB substrate was added to each well and incubated for 30 min. Finally, 50 μL of stop solution was added to each well and gently tapped the plate to ensure thorough mixing. The optical density at 450 nm of each well was measured within 5 min. All processes were performed at 37 °C in a dark room.

2.6. ELISA assay for APOA2 protein quantification

10 μg mL^{-1} Anti-APOA2 (150 μL) were coated on Microlite 2 multiwell plates (Thermo Labsystems, Franklin, MA) for 1.5 h. After washing with PBS, 150 μL of BSA (5 mg mL^{-1}) were used as block for 1.5 h before hybridization with 55.7, 24.8, 12.9, 6.5, 3.2, 1.6 and 0.8 ng mL^{-1} of APOA2 protein (150 μL) for 1.5 h. A total of 150 μL of BSA (5 mg mL^{-1}) were utilized for further blocking. 100 μL of biotin-antibody was added to each well and incubated for 1 h at 37 °C. After removing the solution, 90 μL of TMB substrate was added to each well and incubated for 30 min. Finally, 50 μL of stop solution was added to each well and gently tapped the plate to ensure thorough mixing. The optical density at 450 nm of each well was measured within 5 min. All processes were performed at 37 °C in a dark room.

2.7. ELISA assay for anti-APOA2 activity using Ab-MGLA and Ab-MGSA

100 μL of Ab-MGLA or Ab-MGSA with solid containing 0.5 mg mL^{-1} were coated on Microlite 2 multiwell plates (Thermo Labsystems, Franklin, MA) for 1.5 h. After the liquid solution was removed without washing, 150 μL of BSA (5 mg mL^{-1}) were used as block for 1.5 h before hybridization with 1.95 μg mL^{-1} of APOA2 protein (150 μL) for 1.5 h. A total of 150 μL of BSA (5 mg mL^{-1}) were utilized for further blocking. 100 μL of biotin-antibody was added to each well and incubated for 1 h at 37 °C. After removing the solution, 90 μL of TMB substrate was added to each well and incubated for 30 min. Finally, 50 μL of stop solution was added to each well and gently tapped the plate to ensure thorough mixing. The optical density at 450 nm of each well was measured within 5 min. All processes were performed at 37 °C in a dark room and under an additional magnetic field.

2.8. Bio-Plex assay for APOA2 protein quantification in individual urine samples

The urine level of APOA2 apolipoprotein was determined with the MILLIPLEX MAP Human Apolipoprotein Panel kit (Millipore, MA, USA) using the Bio-Plex system (Bio-Rad Laboratories), as previously reported (Chen et al., 2013a). The assay procedure was a modification of the blood sample-suitable protocol provided by Millipore. The immunobeads were analyzed using the Bio-Plex 200 system (Bio-Rad Laboratories). Standard curves and analyte concentrations were obtained using Bio-Plex Manager software version 4.2 (Bio-Rad Laboratories). In total, 20 urine samples (10 from hernia patients, 10 from patients with bladder cancer) were analyzed using the Human Apolipoprotein Kit, which is commercially available as a 96-well plate immunoassay. The details of measurements using the Bio-Plex assay are provided in Supporting information.

2.9. Fabrication of poly-SiNW-FET

The sample nanowire devices were manufactured on standard six-inch p-type wafers (Fig. 1A). Initially, a buried oxide/nitride layers were deposited onto the substrate surface as the gate dielectric of the nanowire FETs to avoid surface reaction species penetrating to substrate gate. A 50-nm polysilicon layer was then deposited *via* chemical vapor deposition. The poly-Si wire was subsequently patterned using a standard I-line stepper from the CMOS semiconducting process. The photoresist was trimmed using reactive plasma etching followed by Si etching, and the nanowire dimensions were reduced to approximately 0.3 μm. A channel protection photoresist pattern was then formed *via* I-line lithography. Channel protection patterning was performed both to prevent the channel from intrinsically implanting the n^+ source/drain (S/D) and to increase the field sensitivity of the nanowire. The n^+ S/D was subsequently implanted using a 10^{15} cm^{-2} $P_{31}{}^+$ ion beam at 10 keV to reduce the parasitic resistance of the nanowire. Then, the channel protection photoresist was removed. Finally, the S/D dopant was activated by annealing at 600 °C for 30 min under a N_2 atmosphere. A thick SiN_x passivation layer was deposited onto the wafer to protect the Si substrate gate from damage by the solutions used during pH testing. This n-type poly-SiNW-FET fabrication requires only two additional masks and can be integrated with a conventional 0.35 μm CMOS process. The morphology of poly-SiNW channel is shown in Fig. 1B.

2.10. Modification of poly-SiNW-FET and fabrication of the biochip

The functional modification of the poly-SiNW-FET with terminal amine groups was performed as follows. A 5- μL solution of 2 wt% APTES in ethanol was placed on the poly-SiNW for 1 h to form a self-assembled monolayer. The modified chip was then washed with ethanol and dried in an oven at 100 °C for 1 h. To add the Ab-MGLA or Ab-MGSA, the chip was further treated with 5% glutaraldehyde at room temperature for 1 h, resulting in the formation of terminal aldehyde groups for direct immobilization after the addition of Ab-MGLA or Ab-MGSA to poly-SiNW-FET for 1 h. Finally, 5 μL of BSA (5 mg mL^{-1}) in PBS was added at 4 °C for 1 h in the dark to block non-specific binding, followed by washing with PBS three times before use for further detection.

2.11. APOA2 protein detection on Ab-MGLA/poly-SiNW-FET and Ab-MGSA/poly-SiNW-FET

We used the response current of the FET in 0.5 mM PBS as the baseline current. The APOA2 protein standard was injected into the microfluid channel and reacted for 10 min in the dark at room

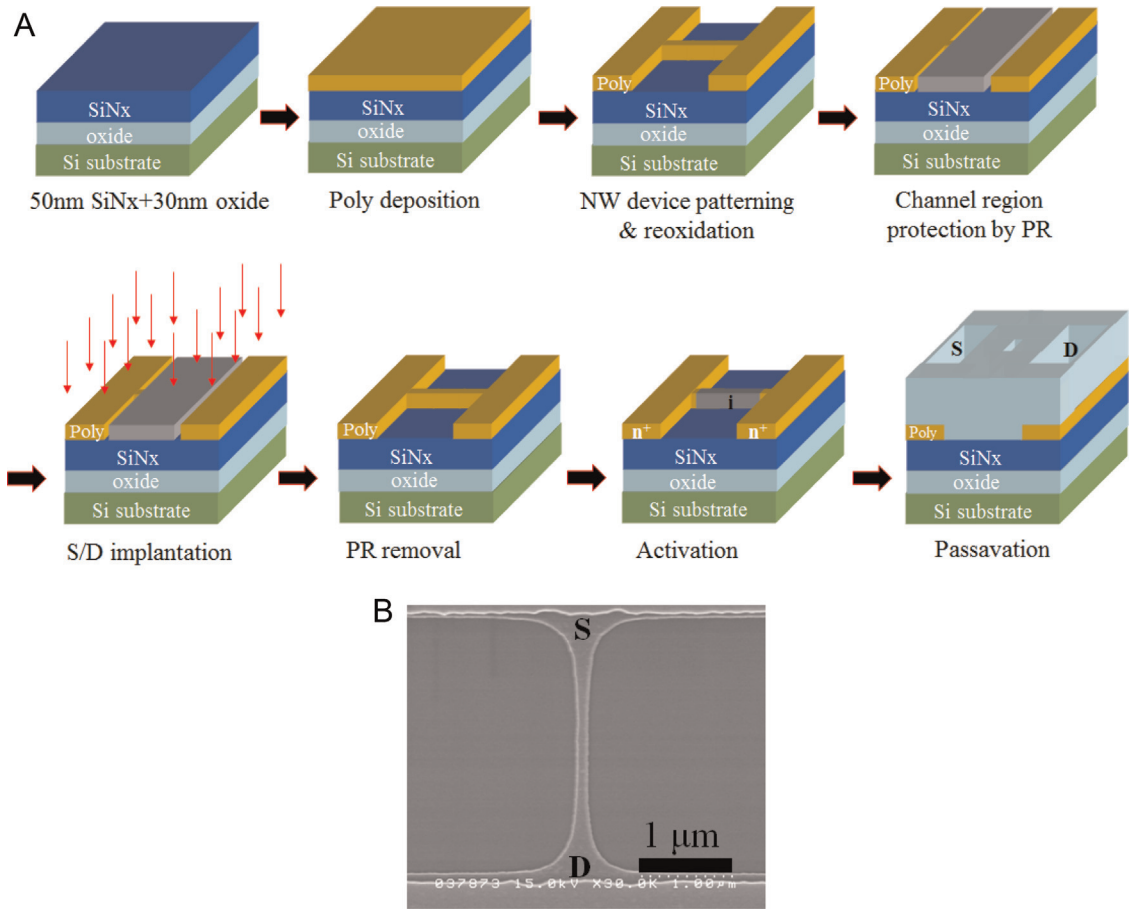

Fig. 1. (A) Schematic representation of poly-SiNW-FET device fabrication and (B) SEM image of a typical poly-SiNW-FET device.

temperature. The unreacted APOA2 protein was removed by washing three times, and PBS was re-injected into the microfluid channel prior to measurement. Similarly, APOA2 detection in individual urine from patients suffering from bladder cancer was performed according to the above reacting, washing and measuring processes. The measured volumes of the samples were 5 μL. All measurements were obtained using a 50-mV bias voltage, V_B. We chose a current at a constant gate voltage (V_G=3.0 V) as the criterion to quantify the APOA2 protein.

2.12. Characterization methods

To characterize GLA, GSA, MGLA and MGSA, FT-IR spectra were obtained using a Bruker-Tensor 27 spectrometer at a spectral resolution of 8 cm^{-1}. The presence of exfoliated Gs was confirmed by XRD patterns, obtained using a Rigaku D/Max-2B with nickel-filtered Cu K_α radiation at a scanning rate of 1° min^{-1} and scanning range from 5° to 90°. TEM images were obtained using a Hitachi H-7500 system. Field-emission scanning electron microscopy (FE-SEM) was performed using a Hitachi S-5000 system. Absorption spectra were recorded on a Perkin-Elmer Lambda 800/900 spectrometer. XPS measurements were obtained using a VG Scientific ESCALAB 250 system.

3. Results and discussion

3.1. Characterization of GLA

Fig. S1 shows the synthetic scheme of carboxylated graphene with long-chain acid groups (GLA) from pristine graphite *via* Friedel–Crafts chemical acylation using $AlCl_3$ as the catalyst to perform maleic anhydride (MA) ring opening. After 48 h of reaction, carboxylated graphene with short-chain acid groups (GSA) obtained by either Hummers' method or GLA was well dispersed in aqueous solution compared to graphite (Fig. S2, inset), indicating the presence of a hydrophilic group (acid group). To determine the optimal reaction conditions, various molar ratios of MA and $AlCl_3$ were examined. As shown in Fig. S2, GLA13 (MA/$AlCl_3$ is 1/3) exhibited absorption peaks at 226 nm, corresponding to the π–π* transition of the aromatic C=C band and the *n*–π* transition of the C=O band (Chen et al., 2013b). Additionally, the absorbance of the broad band extending to 900 nm was higher than that observed for the other two conditions. Inadequate catalyst led to a lower degree of modification, while excess catalyst increased the viscosity of the solution, hindering reactive collisions and thereby also decreasing the degree of modification. Additionally, the absorption intensity of GLA at wavelengths greater than 300 nm increased more significantly than for GSA, indicating that GLA has a greater degree of conjugation than GSA. In Hummers' method, the addition of a strong oxidizing agent destroys the plane and edge structure and forms acid groups, including other oxygen groups; however, in Friedel–Crafts acylation, electrophilic aromatic substitution occurs on the structure with the highest electron density (edge site). Thus, GLA retains a natively conjugated structure.

The degree of destruction of the conjugated structure was examined by X-ray photoelectron spectroscopy (XPS). The C1s spectrum of pristine graphite was deconvoluted into two peaks, which correspond to the aromatic ring (C=C/C–C) at 284.6 eV and the original defective structures of hydroxyl and epoxy/ether groups (C–O–C) at 286.1 eV (Fig. S3) (Roldán et al., 2012). The

degree of defective structure was determined by calculating the ratio of the area of defective structure to the total area, yielding a value of 14.0%. Similarly, GLA was deconvoluted into two peaks at 287.7 eV (C=O of ketone) and 288.9 eV (O–C=O) with area ratios of 8.7% and 8.7%, respectively (Fig. S4) (Hua et al., 2012). This result is consistent with the theoretical value for 1-one-butenoic acid, which is the chain derived from MA ring opening. Compared with graphite, the degree of defective structure did not significantly increase, indicating that the conjugated structure remained nearly complete.

To further confirm the structural modification, Fourier-transform infrared (FT-IR) spectroscopy was performed on the synthesized GLA (Fig. S5). The typical band characteristic of graphite at 1530 cm^{-1} was assigned to the stretch vibration of C=C ($\nu_{C=C}$). After Friedel–Crafts acylation, GLA13exhibited several new peaks at 1703 cm^{-1} ($\nu_{C=O}$), 1613 cm^{-1} ($\nu_{C=C}$ of graphene overlapping the $\nu_{C=O}$ of the ketone), 1445 and 1264 cm^{-1} (coupling between the in-plane O–H bending and the C–O stretching of the dimer), and 1375 cm^{-1} (–CH_2 bending) (Hua et al., 2011b). Peaks characteristic of the asymmetric and symmetric $\nu_{C=O}$ of MA were not observed at 1869 or 1777 cm^{-1}, confirming MA ring opening and 1-one-butenoic acid formation at the edge site. The presence of the acid chain facilitates the dispersion of GLA in aqueous solution due to the negative charge repulsion of the anion generated by dissociation.

Toluidine blue O (TBO) was used as a probe to quantify the carboxylic group density based on the absorption spectrum at 633 nm (Pistillo et al., 2011). As shown in Fig. S6, GLA13 exhibited the highest carboxylic group density (1.33×10^{-6} mol mg^{-1}), confirming the optimal reaction conditions and the presence of carboxylic groups. This value is also higher than that of the graphene oxide (0.38×10^{-6} mol mg^{-1}) obtained *via* Hummers' method.

The stability of the carboxylic side chain was confirmed by thermal gravimetric analysis (TGA) from 100 °C to 690 °C (Fig. S7). Due to the high strength of the graphite structure, little weight loss was observed. However, both GLA and GSA exhibited significant weight loss due to the destruction of the structure during chemical modification and the instability of the side chain. GSA initially exhibited weight loss due to the thermal degradation of the side chain at approximately 100 °C. Compared to GSA, GLA exhibited higher thermal stability, with initial weight loss occurring at 240 °C, indicating that enhanced preservation of the graphene structure improved side chain stability. Additionally, the total weight loss of GLA was greater than that of GSA, revealing a high molecular weight and high degree of grafting to the 1-one-butenoic acid group.

Further, the conformation of GLA was analyzed by XRD in the presence of nickel powder (15% wt/wt), which yielded diffraction peaks at 44.8°, 52.2° and 76.7°, and was used as a normalization standard (Fig. S8) (Chen et al., 2013b). Graphite exhibits two strong diffraction peaks at 26.9° and 55.0° due to crystalline heavy stacking. In contrast, for GLA, the former peak decreases in size and shifts to a lower angle, while the latter peak disappears. These results indicate that the heavy stacking sheet is destroyed due to exfoliation into graphene, which increases the associated *d*-space. Additionally, TEM analysis revealed a transparent thin sheet with a wrinkled appearance (Fig. S9), which is in agreement with the structural features of a graphene sheet. This result demonstrates that graphite can be functionalized and exfoliated into grapheme *via* Friedel–Crafts chemical acylation.

3.2. Characterization of MGLA

For size compatibility with the poly-SiNW-FET, the relatively large synthesized GLA was miniaturized using an ultrasonic process; next, the GLA was magnetized through the *in situ* synthesis of Fe_3O_4 nanoparticles on its surface. Fig. 2A shows that MGLA was miniaturized to approximately 40 nm and was covered with nanoparticles, which were 5 nm in size. Moreover, no free nanoparticles were observed either within or dispersed around the composite. These results indicate that the nanoparticles were adsorbed on GLA, while free nanoparticles were displaced during purification.

Compared with the absorption bands of GLA and GSA, a new shoulder, corresponding to the Fe_3O_4 nanoparticles, was observed at approximately 400 nm in MGLA and MGSA (Fig. 2B) (Yang et al., 2013). This result demonstrates that the nanoparticles on the GLA surface are Fe_3O_4, confirming the synthesis of MGLA. The photo also confirms that the MGLA composite is magnetic (Fig. 2B inset). MGLA was further characterized by XRD. Six new diffraction peaks at 30.4°, 35.8°, 43.5°, 53.7°, 57.3° and 63.1° were attributed to the crystalline Fe_3O_4 (Fig. 2C). Additionally, FT-IR spectroscopy revealed the characteristic peak of Fe–O at 584 cm^{-1} in MGLA, which is a slight red shift on the order of 2 cm^{-1}compared to Fe_3O_4 NPs. This result reveals that interactions between GLA and Fe_3O_4 increase adsorption (Fig. S10).

The magnetization of GLA to MGLA increased from 0 to 51.0 emu g^{-1} (Fig. 2D). However, MGSA exhibited higher magnetization (61.0 emu g^{-1}) than MGLA. The increased magnetization of MGSA is most likely due to the destruction of the GSA structure and associated oxygen groups, favoring the adsorption of Fe_3O_4 NPs. Additionally, the carboxylic group densities of MGLA and MGSA after magnetization decreased significantly to 0.17×10^{-6} mol mg^{-1} and 0.08×10^{-6} mol mg^{-1}; this finding suggests that the highly alkaline solution used during the magnetizing process cleaved the acid chain (Fig. S11).

3.3. Quantification of urinary APOA2 and clinical importance for bladder cancer

We previously demonstrated that the average urinary concentration of the APOA2 protein was approximately 3.0–78.4-fold higher in bladder cancer patients at different stages than in non-tumor controls, as determined using a mass spectrometry (MS)-based platform and a Western blot assay (Chen et al., 2010, 2012). The quantification of a protein marker using a MS platform is specific and *multiplexable* but requires costly instrumentation that may not be affordable for common laboratories and clinics. As part of the biomarker development pipeline, a potential biomarker discovered or verified in academia should be further translated to the clinic using a high-throughput, sensitive immunoassay to quantify the target protein in a large number of clinical samples (Surinova et al., 2011; Solier and Langen, 2014). Fig. 3A shows that the higher urinary concentration of APOA2 in bladder cancer patients was confirmed by an immune-based Bio-Plex system in a larger number of samples with statistical significance (54.5-fold higher, $n=111$, $p<0.001$, area under the curve (AUC)=0.864) (Chen et al., 2013a). To further address the problems of tedious workflow for urine sample preparation using the Bio-Plex system while improving the sensitivity of detection, we explored the quantification performance of urine APOA2 protein using the Ab-MGLA/poly-SiNW-FET-based biosensor.

3.4. Immobilization and characterization of Ab-MGLA

The immobilization of ananti-APOA2 antibody (Ab) on MGLA was accomplished using EDC/sulfo-NHS as the linker to form a bioconjugate bond between Ab and MGLA. Ab is specific for the AOPA2 protein. The immobilized Ab and its bioactivity were quantified using an enzyme-linked immunosorbent assay (ELISA). The optimal loading on 1 μg of MGLA was examined by reaction

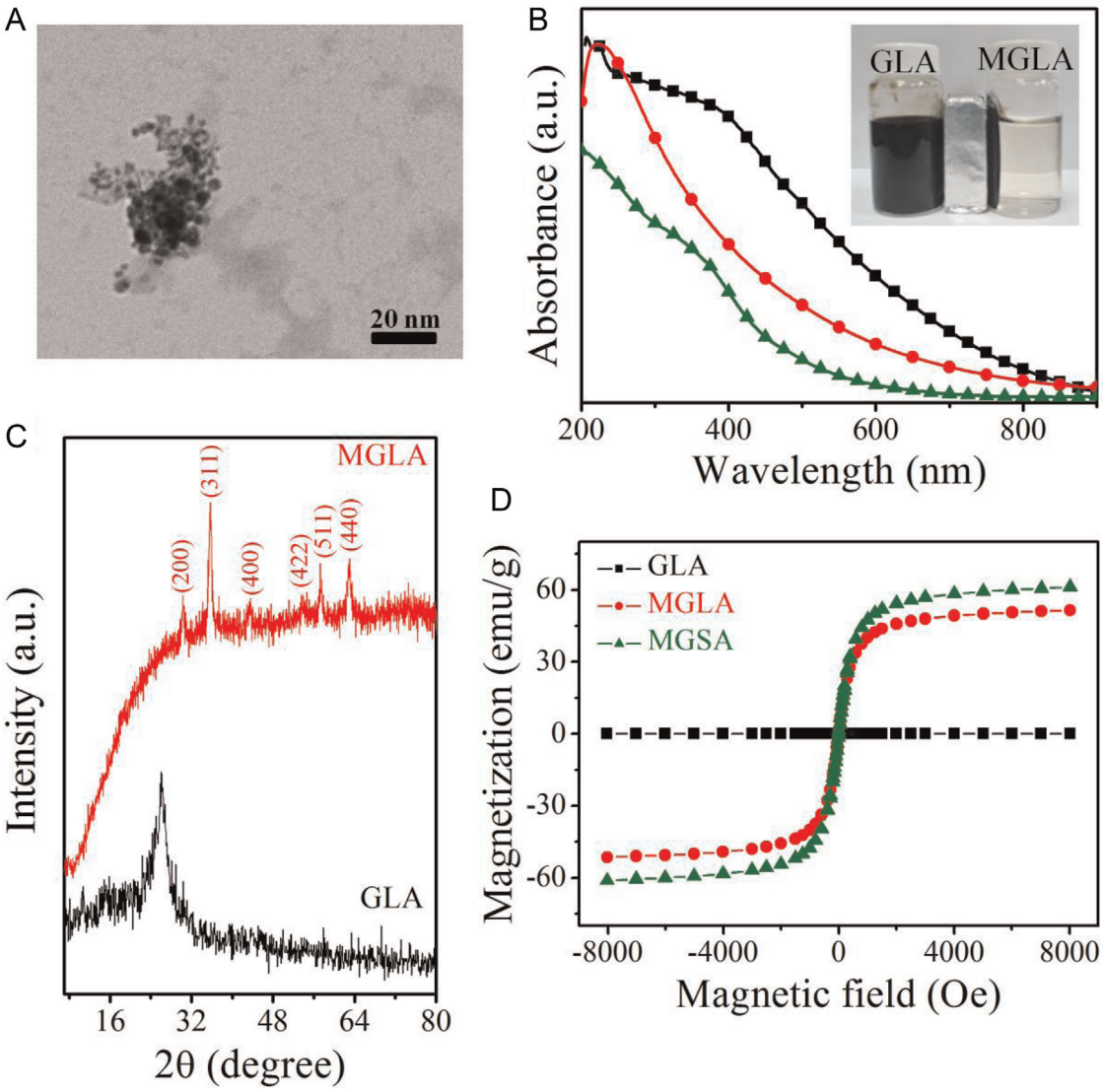

Fig. 2. (A) TEM analysis of MGLA. (B) The absorption spectra of (▲) Fe_3O_4 NPs, (●) GLA, and (■) MGLA. Inset: Photos of GLA and MGLA obtained under an applied magnetic field. (C) The XRD spectra of GLA and MGLA. (D) The magnetization curves of GLA, MGLA, and MGSA.

with various concentrations of Ab. The loaded quantity of Ab was calculated by ELISA of the un-immobilized Ab at a monitoring wavelength of 450 nm (Fig. 3B and C). The optimal amount of Ab immobilized on 1 μg of MGLA was approximately 42 ng. The degree of immobilization was 1.4%, in which MGLA provided 1.7×10^{-10} mol of carboxylic groups to load 2.4×10^{-12} mol of Ab (17.4 kDa) (Fig. 3D). To investigate the effect of chain length, MGSA (2.13 μg) containing the same quantity of carboxylic groups was also loaded with Ab. However, the optimal amount of Ab immobilized on 2.13 μg of MGSA was approximately 29 ng. The degree of immobilization was 0.98%, such that MGSA provided 1.7×10^{-10} mol of carboxylic groups to load 1.67×10^{-12} mol of Ab. The quantity of immobilized Ab was 1.43-fold higher on MGLA than on MGSA. This result indicates that the longer chain, which has more degrees of freedom, can overcome the steric hindrance within the large biomolecule during immobilization. The activity of the immobilized Ab, which is the dominant factor in biosensor performance, was also investigated. The retained activity of the immobilized Ab on MGLA was approximately 71% as determined by ELISA (Fig. 3C), while 62% activity was observed on MGSA. The immobilized Ab fraction on MGSA was likely confined to the surface in clusters. As proteins are introduced, the very large proteins (37 kDa) are subject to steric hindrance among themselves. The negatively charged proteins are subject to charge repulsion, increasing the difficult of targeting and decreasing the bioactivity of the material. In contrast, the long chain can extend and bend at random angles to produce a large space for protein targeting, resulting in higher bioactivity.

3.5. Preparation and characterization of Ab-MGLA/poly-SiNW-FET biosensors

The development of a poly-SiNW-FET biosensor depends on the measurement of the variation in conductance, which is induced by disturbing the surface charge. Therefore, poly-SiNW-FET with a wire length of 2 μm and a width of 0.15 μm was used as the biochip to fabricate the Ab-MGLA/poly-SiNW-FET biosensor (Fig. 1B). Considering the limitation of the Debye length, the direct deposition of Ab-MGLA on poly-SiNW was excluded. To fabricate the thinnest possible layer of Ab-MGLA on the poly-SiNW, the surface of poly-SiNW first must be modified by (3-aminopropyl) triethoxysilane (APTES) and glutaraldehyde (GA) to provide terminal aldehyde groups that can form covalent bonds with Ab-MGLA (Fig. 4A). Unmodified sites are blocked by bovine serum albumin (BSA) to prevent non-specific reactions or binding. The efficient detection range of a FET biosensor is within the Debye

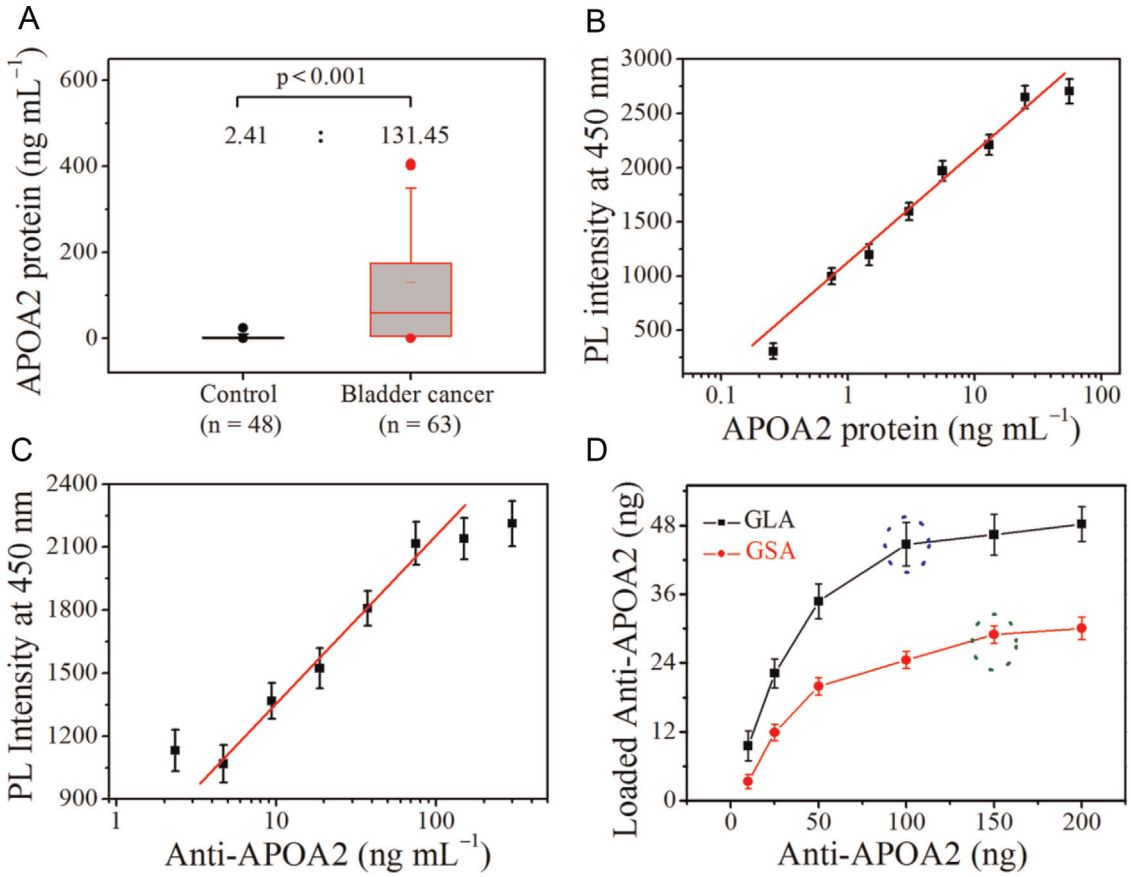

Fig. 3. (A) Validation of APOA2 using a multiplexed Bio-Plex assay. The concentration of urinary APOA2 was elevated in bladder cancer patients compared to hernia patients (total $n=111$). The optical density (O.D.) calibration curve for (B) APOA2 protein and (C) anti-APOA2 concentrations based on ELISA ($n=3$). (D) The optimization of anti-APOA2 immobilization ($n=3$).

length, which is associated with the ionic strength of the solution. Although a higher ionic strength results in a shorter Debye length, the FET exhibits higher sensitivity. TEM analysis revealed that MGLA was approximately 40 nm wide and 11 nm thick, assuming that the thickness of GLA is 1 nm and that two Fe_3O_4 NPs are located on the top and bottom of the GLA plane. Therefore, the use of 0.5 mM PBS with a Debye length of approximately 15.2 nm is suitable. The optimal conditions for Ab-MGLA loading were investigated by reacting with various concentrations of Ab-MGLA, ranging from 0.025 to 1 μg mL^{-1} and corresponding to 1 ng mL^{-1} protein (Fig. 4B). The current of the Ab-MGLA/poly-SiNW-FET biochip decreased with increasing concentration of Ab-MGLA in the reaction. The relative current change ($-\Delta I/I_0$, %) at each concentration of Ab-MGLA in the reaction was 6.3% at 0.025 μg mL^{-1}, 11.3% at 0.125 μg mL^{-1}, 22.6% at 0.625 μg mL^{-1}and 23.6% at 1.0 μg mL^{-1}. The relative current increases slightly after 0.625 μg mL^{-1}, indicating that the modification was saturated. These results also indicate that the protein was negatively charged. The protein attracted carriers from the substrate to the channel and decreased the conductance between the source and drain electrodes, resulting in decreased conductance.

3.6. *Performance of Ab-MGLA/poly-SiNW-FET biosensors for the detection of protein*

Recent reports of biosensors based on FETs have been developed for real-time detection after the injection of specific analytes, such as proteins or viruses (Oh et al., 2010; Huang et al., 2010). However, FET sensitivity is charge-dependent, such that the current or conductance of FET changes when the analytes are within the Debye length. The change is also affected by other charged species, particularly smaller components, that are nearly physically adsorbed on the FET surface during the measurement of unknown samples, resulting in decreased selectivity. Moreover, the presence of unknown species dissolved in solution also changes the ionic strength and Debye length, varying the current response. Fig. 5A shows the results for Ab-MGLA/poly-SiNW-FET after injection with immunoglobulin G (IgG, 1000 ng dL^{-1}), immunoglobulin M (IgM, 192.5 mg dL^{-1}), glucose (5 mM), ascorbic acid (AA, 4.3 μg mL^{-1}), and uric acid (UA, 0.295 mM) at concentrations typically found in human plasma. These species were also studied at concentrations that were twice as large as the values listed above. The injection of either normal or excess concentrations of species changed the current. However, the major variations were reduced when the solutions were removed, followed by washing and the injection of pure buffer. Although the currents differed slightly from those in the presence of PBS, due to either the limited adsorption of species or the interference of Ab-protein binding as a result of the species present, washing the FETs before carrying out the measurement eliminated most of the interference. To evaluate the effect of protein binding in the presence of key interfering species, 1 ng of protein was hybridized in the presence of each of the species identified above (Fig. 5B). In addition to species adsorption, the slight differences observed relative to the pure protein solution demonstrates the presence of interfering species and indicates that interactions between the protein and interfering species affects protein binding. The changes in the current are dependent on the quantity of bound protein, which can be exploited to improve selectivity.

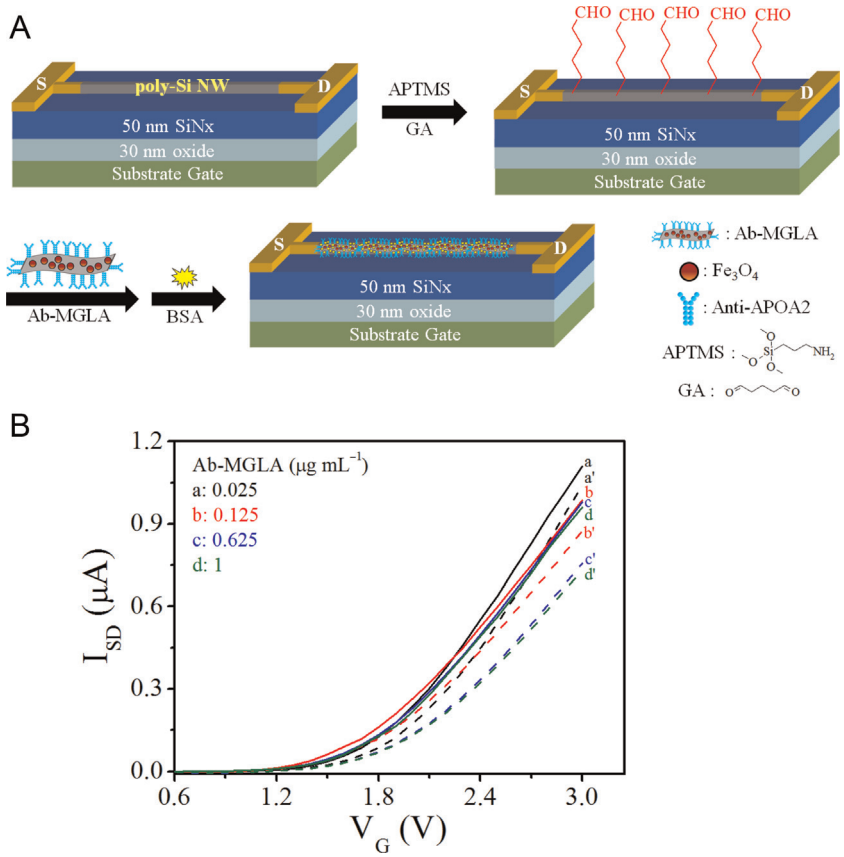

Fig. 4. (A) A schematic of the process of poly-SiNW-FET device surface modification and Ab-MGLA/poly-SiNW-FET biosensor preparation. (B) I_{SD}–V_G curves of the reaction of [Ab-MGLA] with a, b, c, and d and the corresponding I_{SD}–V_G of a′, b′, c′ and d′ under 1 ng mL^{-1} protein binding.

The process of protein binding, washing and measuring was used to assess the performance of the Ab-MGLA/poly-SiNW-FET biosensor under different concentrations of protein. The current decreased with increasing protein concentration due to the depletion of charge carriers in the poly-SiNW-FET, while the negatively charged protein remained bound to the Ab-MGLA surface (Fig. 5C).The relationship between I_{SD} and the protein level reveals that the relative current change increased proportionally with increasing protein fraction from 19.5 pg mL^{-1} to 1.95 μg mL^{-1} (Fig. 5D). Compared with Ab-MGLA/poly-SiNW-FET, the biosensor based on Ab-MGSA/poly-SiNW-FET exhibited a linear dependence of relative response to the logarithmical concentration in a range of from 195 pg mL^{-1} to 19.5 μg mL^{-1}, with a lower slope that corresponded to lower sensitivity. The limit of detection (LOD) of Ab-MGLA/poly-SiNW-FET and Ab-MGSA/poly-SiNW-FET were calculated using $3\sigma S^{-1}$ as previously described (Palaniappana et al., 2010), where σ is the standard deviation of device in pure buffer solution and S indicates the sensitivity (slope) of the device at lower concentrations. The standard deviations of Ab-MGLA/poly-SiNW-FET and Ab-MGSA/poly-SiNW-FET in the absence of APOA2 were 0.88% and 0.71%, respectively. The LOD of Ab-MGLA/poly-SiNW-FET and Ab-MGSA/poly-SiNW-FET can be estimated through $3\sigma S^{-1}$ and were 6.7 pg mL^{-1} and 95.9 pg mL^{-1}, respectively. In addition, the time of analysis is dependent on the scan rate. In this study, the scan range was between 0 and 3 V with a scan rate of 0.5 V s^{-1}, resulting in a response time of 6 s. The superior performance of the Ab-MGLA/poly-SiNW-FET biosensor can be attributed to the higher amount of bioactive sites and lower steric hindrance with respect to protein binding.

Additionally, the stability of each biosensor type was investigated after dry storage at 4 °C for one week. The relative currents for 1 ng mL^{-1} protein decreased by approximately 20.2% for Ab-MGLA/poly-SiNW-FET and 19.5% for Ab-MGSA/poly-SiNW-FET after one week of storage, compared to the values obtained for fresh biosensors. The immobilized fractions of Ab on MGLA/poly-SiNW-FET and MGSA/poly-SiNW-FET perform the stable property.

3.7. Determination of APOA2 protein in human urine

The APOA2 protein is a bladder cancer biomarker that is exhibited in higher concentrations in biofluids (Chen et al., 2010, 2012). Therefore, the performance of the Ab-MGLA/poly-SiNW-FET biosensor developed for clinical analysis was evaluated by examining urine samples collected from bladder cancer patients. In hernia patients, the serum level of protein is 0.425–9.47 ng mL^{-1}, which is significantly lower than the concentration of 29–344 ng mL^{-1} that is typically observed in patients suffering from late- and advanced-stage bladder cancer (Fig. 6). These results demonstrate that the developed Ab-MGLA/poly-SiNW-FET biosensor can be used to distinguish protein levels in hernia and bladder cancer patients. The results of the biosensor are also in agreement with those measured by Bio-Plex, indicating that the diagnosis of bladder cancer based on the developed Ab-MGLA/poly-SiNW-FET is feasible and accurate. Our assay is less complex and time-consuming than the Bio-Plex technology. Differently from cystoscopy, the Ab-MGLA/poly-SiNW-FET biosensor is non-invasive and can limit patient pain and discomfort. Compared with urine cytology, the proposed methodology is operator-independent and can offer a higher sensitivity and diagnostic accuracy. Although subject to future validation, our novel APOA2 biosensor based on Ab-MGLA/poly-SiNW-FET may open new perspectives in bladder cancer diagnostics.

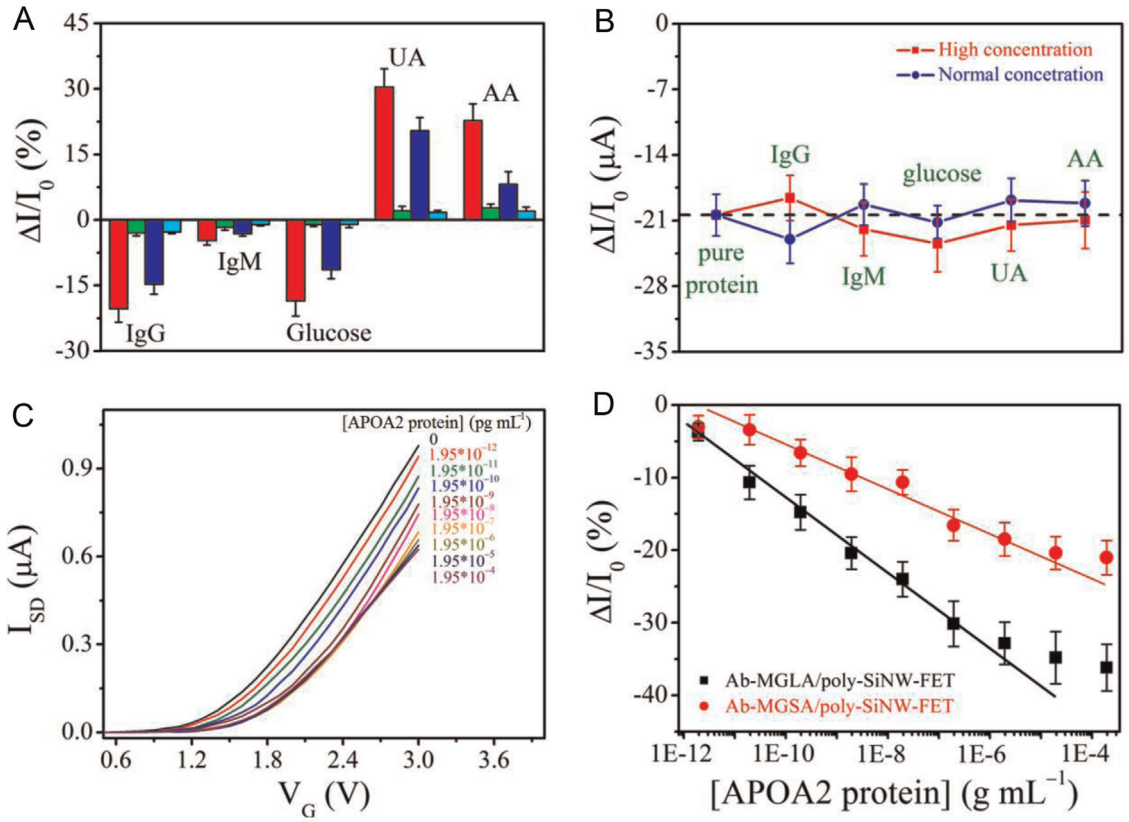

Fig. 5. (A) The effects of interfering species (red bar: high concentration; blue bar: normal concentration) on the current variations in Ab-MGLA/poly-SiNW-FET biosensors before (red and blue bars) and after washing (green and cyan bars) ($n=3$). (B) The effects of interfering species for 1 ng mL^{-1} protein binding. (C) I_{SD}–V_G curves of the Ab-MGLA/poly-SiNW-FET biosensor at various protein concentrations. (D) The calibration curves of the current responses to various protein concentrations for the Ab-MGLA/poly-SiNW-FET biosensor and Ab-MGSA/poly-SiNW-FET biosensor ($n=5$). (For interpretation of the references to color in this figure legend, the reader is referred to the web version of this article.)

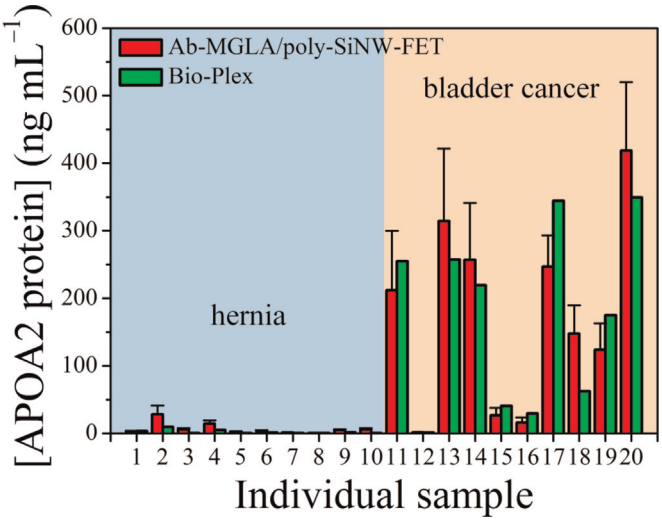

Fig. 6. APOA2 protein concentrations in urine samples from hernia and bladder cancer patients based on Ab-MGLA/poly-SiNW-FET (red bars) and Bio-Plex (green bars) ($n=3$). (For interpretation of the references to color in this figure legend, the reader is referred to the web version of this article.)

4. Conclusions

A label-free electrical method of APOA2 protein detection was developed based on an Ab-MGLA/poly-SiNW-FET biochip. The magnetized MGLA accelerated purification during the immobilization of anti-APOA2, thus preventing the denaturation of anti-APOA2. Additionally, the longer bioactive chain of MGLA provided more freedom, thereby preventing steric hindrance during the immobilization of anti-APOA2 compared to a shorter chain. ELISA results indicated that the immobilized anti-APOA2 on MGLA retained most of its bioactivity. In summary, the MGLA/poly-SiNW-FET biochip exhibited superior performance compared to the MGSA/poly-SiNW-FET biochip. Further, the analysis of urine samples from bladder cancer patients demonstrated the feasibility of the use of the proposed biosensor to diagnose bladder cancer. Thus, this biosensor exhibits substantial potential for use in clinical diagnosis.

Acknowledgments

We thank the National Science Council of the Republic of China, the Chang Gung Memorial Hospital and the Ministry of Economic Affairs for their financial assistance: NSC 101-2221-E-182-013-MY3, CMRPD2D0081, CMRPD2A0043, NSC 102-2113-M-182-001-MY2, 102-D0607 (GERPD2C0141) and D301AR1H10. We also thank the Chang Gung Memorial Hospital Microscopy Core Laboratory for assistance.

Appendix A. Supplementary material

Supplementary data associated with this article can be found in the online version at http://dx.doi.org/10.1016/j.bios.2014.11.019

References

Allen, B.L., Kichambare, P.D., Star, A., 2007. Adv. Mater. 19, 1439–1451.
Araki, M., Nieder, A.M., Manoharan, M., Yang, Y., Soloway, M.S., 2007. Urology 69, 270–274.
Cao, M., Zhao, L., Chen, H., Xue, W., Lin, D., 2012. Anal. Sci. 28, 451–456.
Chen, Y.T., Chen, C.L., Chen, H.W., Chung, T., Wu, C.C., Chen, C.D., Hsu, C.W., Chen, M. C., Tsui, K.H., Chang, P.L., Chang, Y.S., Yu, J.S., 2010. J. Proteome Res. 9, 5803–5815.
Chen, K.I., Lia, B.R., Chen, Y.T., 2011. Nanotoday 6, 131–154.
Chen, Y.T., Chen, H.W., Domanski, D., Smith, D.S., Liang, K.H., Wu, C.C., Chen, C.L., Chung, T., Chen, M.C., Chang, Y.S., Parker, C.E., Borchers, C.H., Yu, J.S., 2012. J. Proteomics 75, 3529–3545.
Chen, H.C., Chen, Y.H., Chen, S.L., Chern, Y.T., Tsai, R.Y., Hua, M.Y., 2013a. Biosens. Bioelectron. 46, 84–90.
Chen, Y.T., Parker, C.E., Chen, H.W., Chen, C.L., Domanski, D., Smith, D.S., Wu, C.C., Chung, T., Liang, K.H., Chen, M.C., Chang, Y.S., Borchers, C.H., Yu, J.S., 2013b. R. Soc. Chem. 0, 271–314.
Chen, H.C., Qiu, J.T., Yang, F.L., Liu, Y.C., Chen, M.C., Tsai, R.Y., Yang, H.W., Lin, C.Y., Lin, C.C., Wu, T.S., Tu, Y.M., Xiao, M.C., Ho, C.H., Huang, C.C., Lai, C.S., Hua, M.Y., 2014. Anal. Chem. 86, 9443–9450.
Ferreira, C.S.M., Papamichael, K., Guilbault, G., Schwarzacher, T., Gariepy, J., Missailidis, S., 2008. Anal. Bioanal. Chem. 390, 1039–1050.
Hua, M.Y., Lin, Y.C., Tsai, R.Y., Chen, H.C., 2012. J. Mater. Chem. 22, 2566–2574.
Hua, M.Y., Chen, H.C., Chuang, C.K., Tsai, R.Y., Jeng, J.L., Yang, H.W., Chern, Y.T., 2011a. Biomaterials 32, 4885–4895.
Hua, M.Y., Lin, Y.C., Tsai, R.Y., Leu, Y.L., Liu, Y.C., Lai, J.T., 2011b. J. Mater. Chem. 21, 7254–7262.
Huang, S.C., Artyukhin, A., Misra, M., Martinez, J., Stroeve, P., Grigoropoulos, C., Ju, J., Noy, A., 2010. Nano Lett. 10, 1812–1816.
Kałuzna-Czaplinska, J., Jóźwik, J., 2014. TrAC-Trends Anal. Chem. 56, 1–90.
Kandimalla, K., van Tilborg, A.A., Zwarthoff, E.C., 2013. Nat. Rev. Cancer 10, 327–335.
Kim, K.W., Shin, Y., Perera, A.P., Liu, Q., Kee, J.S., Han, K., Yoon, Y.J., Park, M.K., 2013. Biosens. Bioelectron. 45, 152–157.
Kirkali, Z., Chan, T., Manoharan, M., Algaba, F., Busch, C., Cheng, L., Kiemeney, L., Kriegmair, M., Montironi, R., Murphy, W.M., Sesterhenn, I.A., Tachibana, M., Weider, J., 2005. Urology 66, 4–34.
Kwon, O.S., Park, S.J., Hong, J.T., Han, A.R., Lee, J.S., Lee, J.S., Oh, J.H., Jang, J., 2012. ACS Nano 6, 1486–1493.
Lee, H.S., Kim, K.S., Kim, C.J., Hahn, S.K., Jo, M.H., 2009. Biosens. Bioelectron. 24, 1801–1805.
Li, B.R., Chen, C.W., Yang, W.L., Lin, T.Y., Pan, C.Y., Chen, Y.T., 2013. Biosens. Bioelectron. 45, 252–259.
Liu, Z., Robinson, J.T., Sun, X.M., Dai, H.J., 2008. J. Am. Chem. Soc. 130, 10876–10877.
Mourant, J.R., Bigio, I.J., Boyer, J., Conn, R.L., Johnson, T., Shimada, T., Laser, 1995. Surg. Med 17, 350–357.
Oh, J., Chang, Y.W., Kim, H.J., Yoo, S., Kim, D.J., Im, S., Park, Y.J., Kim, D., Yoo, K.H., 2010. Nano Lett. 10, 2755–2760.
Oh, J., Yoo, G., Chang, Y.W., Kim, H.J., Jose, J., Kim, E., Pyun, J.C., Yoo, K.H., 2013. Biosens. Bioelectron. 50, 345–350.
Palaniappan, Al, Goh, W.H., Tey, J.N., Wijaya, I.P.M., Moochhala, S.M., Liedberg, B., Mhaisalkar, S.G., 2010. Biosens. Bioelectron. 25, 1989–1993.
Pistillo, B.R., Perrotta, A., Gristina, R., Ceccone, G., Nardulli, M., d'Agostino, R., Favia, P., 2011. Surf. Coat. Technol. 205, S534–S536.
Roberts, W.S., Davis, F., Holmes, J.L., Collye, S.D., Larcombe, L.D., Morgan, S.L., Higson, S.P.J., 2013. Biosens. Bioelectron. 41, 282–288.
Roldán, L., Santos, I., Armenise, S., Fraile, J.M., Garcïa-Bordejé, E., 2012. Carbon 50, 1363–1372.
Shapiro, A., Gofrit, O.N., Pizov, G., Cohen, J.K., Maier, J., 2011. Eur. Urol. 59, 106–112.
Shin, Y., Perera, A.P., Park, M.K., 2013. Sensor. Actuators B-Chem. 178, 200–206.
Solier, C., Langen, H., 2014. Proteomics 14, 774–783.
Surinova, S., Schiess, R., Hüttenhain, R., Cerciello, F., Wollscheid, B., Aebersold, R., 2011. J. Proteome Res. 10, 5–16.
Sykes, E., Charles, H., 2009. Nat. Chem. 1, 175–176.
Tai, S.P., Wu, Y., Shieh, D.B., Chen, L.J., Lin, K.J., Yu, C.H., Chu, S.W., Chang, C.H., Shi, X. Y., Wen, Y.C., Lin, K.H., Liu, T.M., Sun, C.K., 2007. Adv. Mater. 19, 4520–4523.
Trung, T.Q., Tien, N.T., Kim, D., Jang, M., Yoon, O.J., Lee, N.E., 2014. Adv. Funct. Mater. 24, 117–124.
Yang, H.W., Hua, M.Y., Chen, S.L., Tsai, R.Y., 2013. Biosens. Bioelectron. 41, 172–179.